



ASME Accepted Manuscript Repository

Institutional Repository Cover Sheet

Soheyl

Massoudi

soheyl.massoudi@epfl.ch

First

Last

email

An Integrated Approach to Designing Robust Turbocompressors on Gas Bearings through
ASME Paper Title: Surrogate Modeling and Constrained Multi-Objective Optimization

Authors: Soheyl Massoudi, Cyril Picard, Jürg Schiffmann

Proceedings of the ASME 2023 International Design Engineering Technical Conferences and
ASME Journal Title: Computer and Information in Engineering Conference

Volume/Issue 3B: 49th Design Automation Conference Date of Publication (VOR* Online) November 21, 2023

<https://asmedigitalcollection.asme.org/IDETC-CIE/proceedings-abstract/IDETC-CIE2023/87318/1170577>
ASME Digital Collection URL:

DOI: <https://doi.org/10.1115/DETC2023-115201>

*VOR (version of record)

AN INTEGRATED APPROACH TO DESIGNING ROBUST TURBOCOMPRESSORS ON GAS BEARINGS THROUGH SURROGATE MODELING AND CONSTRAINED MULTI-OBJECTIVE OPTIMIZATION

Soheyl Massoudi^{1,*}, Cyril Picard², Jürg Schiffmann¹

¹Laboratory for Applied Mechanical Design
 Ecole Polytechnique Fédérale de Lausanne (EPFL)
 CH-1015 Lausanne, Switzerland

²Department of Mechanical Engineering
 Massachusetts Institute of Technology
 Cambridge, Massachusetts, 02139

ABSTRACT

Designing turbocompressors is a complex and challenging task, as it involves balancing conflicting objectives such as efficiency, stability, and robustness against manufacturing deviations. This paper proposes an integrated design methodology for turbocompressors supported on gas bearings, which utilizes surrogate models and ensemble learning with artificial neural networks. The proposed approach addresses the limitations of nominal and separate optimizations by integrating all relevant design aspects into a single optimization problem. A multi-objective optimization is carried out, considering four objectives and over twenty constraints, including robustness against manufacturing deviations of the radial and axial bearings in terms of stability, load capacity, and efficiency, as well as robustness against performance metric gradients. The proposed methodology maximizes the compressor's range in speeds and mass flow, while also maximizing the signal-to-noise ratio of the isentropic efficiency over the compressor map. Additionally, the approach maximizes system efficiency, taking into account component losses and isentropic efficiency of the compressor. To enable rapid and automated integrated design, the methodology reduces the compressor representation to a fully cylindrical representation. The study finds that the proposed methodology has the potential to significantly enhance the overall performance of turbocompressors in terms of efficiency, stability, and robustness. The methodology eliminates the need for sequential and iterative design steps, providing an optimal starting point for higher representation of the system with CFD and finite elements study. Furthermore, the proposed methodology has broad applications, including the optimization of other complex and interdependent systems in various fields. This study highlights the crucial role of a comprehensive

and integrated approach to turbocompressor design and provides a valuable framework for future research in this area.

Keywords: Herringbone grooved journal bearings, gas bearings, micro-turbomachinery, integrated design, robust design, constrained multi-objective optimization, artificial neural networks

NOMENCLATURE

Roman letters

A	Bearing front
B	Bearing rear
D	Bearing diameter [m]
\dot{E}	Power [W]
f	Objective function/Performance metric [context dependent unit]
F	Force [N]
G	Geometry field [context dependent unit]
h_g	Groove depth [m]
h_r	Ridge clearance [m]
HV	Measure of feasible region [context dependent unit]
I	Moment of inertia [kg m ²]
k	Sweep sampling [–]
L	Bearing axial length [m]
L_A	Bearing front to center of gravity midplane distance [m]
L_B	Bearing rear to center of gravity midplane distance [m]
M	Rotor mass [kg]
N	Rotational speed [RPM]
P	Pressure [Pa]
R	Bearing radius [m]
S/N	Signal-to-Noise ratio [–]

*Corresponding author: soheyl.massoudi@epfl.ch

S	Search space
T	Temperature [K]
<i>Greek letters</i>	
α	Groove-ridge width ratio [–]
β	Groove angle/Impeller angle [°]
γ	Grooved region ratio [–]
Γ	Logarithmic decrement [–]
δ	Interference [m]
Δ	Variation of a given variable
η	Efficiency [–]
θ	Circumferential coordinate/Angular position of blade [°]
Λ	Compressibility number [–]
μ	Viscosity [Pa s]
Π	Pressure ratio [–]
ρ	Density [kg m ^{–3}]
σ	Stress [N m ^{–2}]
τ	Electromagnetic shear stress/Torque [context dependent unit]
Ω	Angular velocity [rad s ^{–1}]

Superscripts and subscripts

a	ambient
,a	axial
bend	bending
bld	blade
cyl	cylinder
end	sampling end
exp	centrifugal expansion
F	feasible
g	groove
hub	hub
i	i _{th} element
in	inlet
is	isentropic
loss	losses
nom	nominal
p	polar
r	ridge
rob	robust
,r	radial
spl	splitter
start	sampling start
t	transverse
w	weight
–	Dimensionless/Mean

Acronyms

CG	Center of Gravity
COMP	Compressor
EM	Electric Motor
GPU	Graphics Processing Unit
HGJB	Herringbone Grooved Journal Bearing
MAG	Magnet
NGT	Narrow Groove Theory
NSGA	Non dominated Sorting Genetic Algorithm
ROT	Rotor
SGTB	Spiral Groove Thrust Bearing

1. INTRODUCTION

1.1 Nature of the Issue

The design of gas bearing supported turbocompressors is a challenging task that requires the optimization of multiple interrelated components, including the compressor wheel, the axial and radial bearings, and the motor. Traditional design approaches typically involve separate optimizations of individual components, which can lead to suboptimal designs due to inherent trade-offs between performance and robustness. Furthermore, optimizing individual components in isolation may result in infeasible designs, where optimal designs for one component are not compatible with optimal designs for other components.

While integrated design approaches have been proposed for various types of machines, such as robots, automotive control actuators, and small-scale turbocompressors, it is still an under-researched area. Wehner et al. [1] demonstrated the power of integrated design by using soft lithography, molding, and 3D printing to create soft analogs of control systems and power sources for microfluidic-based autonomous robots. Picard and Schiffmann [2] also applied an integrated design approach to automotive control actuators, resulting in an optimized solution with better torque and reduced cost compared to industrial solutions. Schiffmann [3] designed a small-scale turbocompressor for a single-stage heat-pump using an integrated approach, which improved the overall system efficiency. However, this approach did not address the issue of robustness against manufacturing deviations.

To address this gap, researchers have proposed integrating robustness considerations into the optimization process for gas bearing supported turbocompressors [4]. For example, Massoudi and Schiffmann [5] developed a surrogate model based on an ensemble of artificial neural networks multi-objective optimization framework using the logarithmic decrement as a metric of stability. They applied this method to derive guidelines for designing robust gas bearing supported rotors, achieving promising results. However, the authors did not fully integrate the robustness considerations with the integrated design approach for the entire system. Their approach was limited to the design of the radial bearings and part of the rotor geometry.

Given the potential benefits of integrated design and the need for robustness, there is a clear opportunity to merge these two approaches in the design of gas bearing supported turbocompressors.

1.2 Goals and Objectives

The goals and objectives of this paper are 1) an integrated design approach of turbocompressor supported on gas bearings that incorporates surrogate models with ensembles of artificial neural networks in constrained multi-objective optimization including manufacturing deviations, 2) the evaluation of the benefits of such an approach in terms of improved design efficiency, increased overall performance and robustness of the design, and 3) a practical tool for engineers and researchers in the field.

1.3 Scope of the Paper

The aim of this paper is to capitalize on the work of Massoudi and Schiffmann [6] by implementing surrogate models for the

axial dynamics and the compressor. This will allow the integrated design of a complex system that is a gas bearings supported turbocompressor, while considering manufacturing deviations by developing a constrained multi-objective optimization framework for integrated and robust design.

To model the compressor, axial dynamics, and rotordynamics of the system, surrogate models are constructed using ensembles of artificial neural networks. These models not only enable computations to scale on graphics processing units (GPUs) but also significantly reduce computation time. By leveraging these models, thousands of turbocompressor designs can be evaluated in a single optimization pass, even when accounting for manufacturing deviations. This approach offers a powerful means of improving the overall efficiency and reliability of turbocompressors by enabling engineers to consider a much broader range of design options in a timely and cost-effective manner.

The approach outlined in this paper provides a constrained multi-objective optimization framework for achieving a robust and integrated design of gas bearing supported turbocompressors. In particular, the study focuses on demonstrating the feasibility of optimal design for a single-stage, electrically-driven heat-pump compressor that is supported by gas bearings and takes into account manufacturing deviations. The study aims to accelerate the design process, eliminate unnecessary iterations in the preliminary design stages, and ultimately deliver a highly performant and manufacturable solution. The proposed methodology represents a valuable methodology for engineers and researchers in the field of turbocompressor design, providing an efficient means of achieving optimal design objectives while considering critical manufacturing constraints.

2. THEORY

The electrically-driven compressor unit comprises an impeller wheel (COMP), a spiral groove thrust bearing (SGTB) to carry axial loads, herringbone grooved journal bearings (HGJBs), and a synchronous permanent magnet electric motor (EM). Figure 1 depicts the unit and its subsystems alongside a compressor map that illustrates the operating range for a given mass flow, rotational speed, and target pressure ratio. The goal of the compressor is to elevate the inlet pressure to an outlet pressure at maximum isentropic efficiency. During startup and speed mapping, the bearings must remain stable and dissipate minimal energy while providing sufficient load capacity to balance the weight and axial force of the compressor under manufacturing deviations. Surrogate models trained using validated models of the bearings, rotordynamics, and impeller enable a fully integrated and robust optimization of the entire unit. Additionally, fast analytical models or 1D finite element code are utilized to evaluate the losses, load capacities, structural integrity and bending frequency.

2.1 Models

2.1.1 Axial and Journal Bearings. The performance of the axial and journal bearings can be modeled using the Reynolds equation, which is derived from the Navier-Stokes equations under the assumptions of thin-film, laminar flow, and Newtonian fluid.

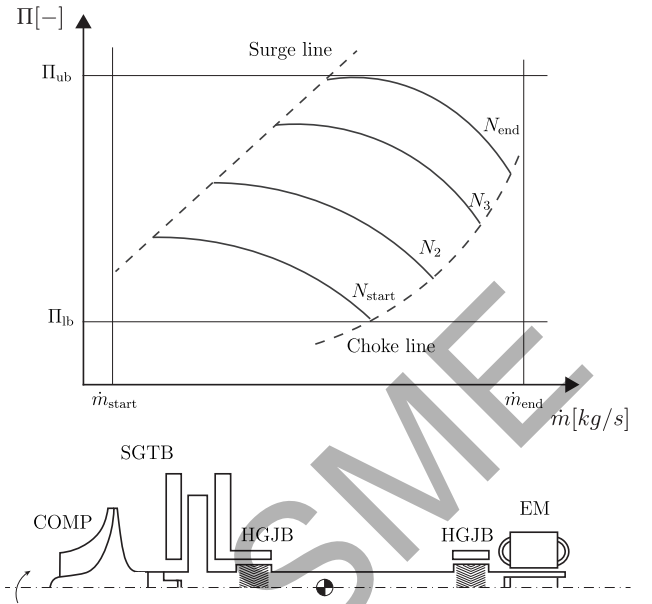


FIGURE 1: COMPRESSOR MAP AND SCHEMATIC OF THE TURBOCOMPRESSOR UNIT. THE COMPRESSOR MAP SHOWS THE RANGE OF OPERATION BETWEEN SURGE AND CHOKE FOR A SAMPLED MASS FLOW, ROTATIONAL SPEED, AND TARGET PRESSURE RATIO. THE SCHEMATIC ILLUSTRATES THE MAIN SUBSYSTEMS OF THE ELECTRICALLY DRIVEN COMPRESSOR UNIT, INCLUDING THE IMPELLER WHEEL (COMP), SPIRAL GROOVE THRUST BEARING (SGTB), HERRINGBONE GROOVED JOURNAL BEARINGS (HGJBs), AND SYNCHRONOUS PERMANENT MAGNET ELECTRIC MOTOR (EM).

The Narrow Groove Theory (NGT) [7] is used to assume that the grooves in the bearings have infinitesimal width. Ideal gas assumption and isothermal compression eliminate the dependence on density. The solution to the Reynolds equation is obtained using perturbation about a concentric position of the bearing, and the zeroth and first order pressure perturbations are determined using numerical integration. The direct and cross-coupled stiffness and damping coefficients can then be obtained from these perturbations. To account for the centrifugal expansion, the radial bearing clearance is adjusted.

2.1.2 Rotordynamics and Axial Dynamics. The rotor and bushings are assumed to be rigid. The stiffness and damping of the gas bearings are functions of the excitation frequency ω_{ex} , which is often different from the system's natural frequency ω_n . To compute the stability of the rigid-body rotordynamic system, the following algorithm is applied for each nominal speed Ω :

Compute the stiffness and damping coefficients of the gas bearings for a range of discrete excitation frequencies $\omega_{ex,i}$:

$$K_i = K(\omega_{ex,i}), \quad C_i = C(\omega_{ex,i}) \quad (1)$$

Form the system matrix $[M][\ddot{q}] + [C][\dot{q}] + [K][q] = [0]$, where $[M]$ is the mass matrix, $[C]$ is the damping matrix, $[K]$ is the stiffness matrix and $[q]$ is the vector of displacement. Compute

the eigenvalues $\delta_i = \lambda_i + j\omega_i$ of the system matrix at each excitation frequency. Compute the logarithmic decrement Γ_i as the metric of stability:

$$\Gamma_i = -\lambda_i \frac{2\pi}{\omega_i} \quad (2)$$

If Γ_i is positive for all excitation frequencies, the system is stable. The system can then be excited in four modes: cylindrical forward (CylF), cylindrical backward (CylB), conical forward (ConF), and conical backward (ConB). The axial dynamics are computed in a decoupled fashion by neglecting the tilting motion for sufficiently long rotors. The system is then treated as a damped point mass oscillator and solved using a similar spectral approach to the rotordynamics analysis.

To compute the bending frequency, a 3-layer composite cylinder model of the rotor is used, which employs 1D finite elements. In this model, each element (or cylinder) is considered as an elastic structure with two nodes and four degrees of freedom per node, which correspond to two displacements and two rotations [8, 9]. The constitutive equation used for the model is based on the Timoshenko beam theory, while Hermitian polynomials are employed to prevent shear locking and to avoid an overestimation of the element stiffness [10]. This approach provides an accurate and efficient way of computing the bending frequency of the rotor, which is an important parameter for assessing the structural integrity of the turbocompressor system.

2.1.3 Compressor. The compressor model used in this study is the Python version [11] of a 1D code developed by Schiffmann and Favrat [12]. This code is based on a meanline model, which is augmented with empirical loss models to capture the effects of fluid flow phenomena. The model is capable of detecting numerical errors, surge, choke, and other abnormal operating conditions. The outputs of the model include pressure ratio, isentropic efficiency, and isentropic enthalpy change for a given set of geometry and operating conditions. A cut view of a typical centrifugal compressor and the geometric variables required for the meanline model are shown in Fig. 2.

2.1.4 Electric Motor. The electric motor chosen for this turbocompressor is a brushless DC motor (BLDC) controlled with pulse-width modulation (PWM). Its size is determined using the electromagnetic shear stress, which is calculated using the formula:

$$\dot{E}_{EM} = 2\pi R_{MAG}^2 L_{MAG} \tau \Omega \quad (3)$$

Here, R_{MAG} and L_{MAG} denote the radius and length of the magnet, respectively, while τ represents the airgap shear stress. This formula helps in calculating the motor power, as described in [13].

2.1.5 Losses. To accurately assess the total energy consumption of the system, analytical models are used to estimate the energy losses in the bearings and electric motor. For the axial bearing, the energy loss is denoted as \dot{E}_{SGTB} , while for each radial bearing, the loss is \dot{E}_{HGJB} . These losses are computed using a laminar flow model that has been experimentally validated [14]. The windage losses in the electric motor, denoted $\dot{E}_{EM,loss}$, are

estimated by discriminating between laminar and turbulent flow regimes using the Taylor number.

The energy loss in each radial bearing can be calculated using the following equation:

$$\dot{E}_{HGJB} = 2\pi R^3 \Omega^2 \left(\frac{\gamma_r \alpha_r}{h_{g,r}} + \frac{1 - \gamma_r \alpha_r}{h_{r,r}} \right) \mu L \quad (4)$$

where R is the radius of the bearing, γ_r the ratio of grooved length to bearing length L , $\alpha_r = a_r / (a_r + b_r)$ the ratio of groove width (a_r) and ridge width (b_r), Ω is the rotational speed in rad s^{-1} , and μ is the dynamic viscosity. $h_{g,r}$ is the groove depth and $h_{r,r}$ is the local bearing clearance. Similarly, the energy loss in the axial bearing can be computed using:

$$\dot{E}_{SGTB} = \mu \frac{\Omega^2 \pi}{2} \left[\left(R_o^4 - R_g^4 \right) \left(\frac{\alpha_a}{h_{g,a}} + \frac{1 - \alpha_a}{h_{r,a}} \right) + \left(R_g^4 - R_i^4 \right) \frac{1}{h_{r,a}} \right] \quad (5)$$

with R_o the outer radius of the thrust bearing, R_i its inner radius and R_g the radius marking the start of the grooved region. Finally, the windage losses in the electric motor can be estimated using:

$$\dot{E}_{EM,loss} = c_w \pi \rho \Omega^3 R_{EM}^4 L_{EM} \quad (6)$$

Here, c_w is a coefficient that accounts for laminar or turbulent flow conditions and ρ is the fluid density. The energy losses in the bearings and electric motor are important to consider, as they contribute to the total energy consumption of the system and can affect its overall performance.

2.1.6 Load capacities. The load capacities of the axial and journal bearings are calculated by solving the perturbed and unperturbed pressure equations and then integrating them over the bearing domains [15]. These equations take into account the dynamic effects of the rotor and the lubricant film. By solving these equations, the maximum loads that the bearings can support without failure can be determined.

2.1.7 Structures. To ensure structural integrity, a composite annulus 2D axisymmetric model of the rotor shaft and its components is used [16]. The model considers the interference between two cylindrical layers of different materials, the centrifugal forces generated by the high-speed rotation of the shaft, thermal dilation, and axial stresses transmitted by the impeller and axial bearing. Additionally, the necessary interference for torque transmission between the magnet and the shaft, and between the plug and rotor is considered, as well as the resulting shear stresses. The model considers two cases: those where interference occurs between two layers of a shaft segment, and those with mono-material without interference.

2.2 Surrogate models

The use of surrogate models is crucial in enabling the scaling of design for system integration and robustness evaluation. However, the increased evaluation of different subsystems, robustness, and complete compressor map leads to a considerable rise in

function evaluations. Consequently, there is a higher number of optimization objectives, design parameters, and evaluations per generation. As a result, several hundred million model evaluations per optimization, if not billions, are necessary, which is impractical and unfeasible without significantly increasing computational resources. To address this challenge, surrogate models are used to replace the baseline models of the bearings, rotor and axial dynamics, the load capacities of the bearing, and the compressor performance prediction. Unlike analytical models for losses and electric motor power estimation, these models cannot be reduced to a matrix representation and element-wise computation. Although the bending frequency is computed using a 1D finite element code, a surrogate model for this analysis is not necessary because the computation is relatively fast and completes in a few milliseconds.

Data is sampled from the baseline models, following the approach proposed by Massoudi and Schiffmann [6]. A combinatorial sampling technique is employed to map a broad range of operating conditions within the gaseous regions of refrigerant fluids, air, and steam, with the aim of deriving the thermodynamic properties of fluids, such as viscosity. Two Latin hypercube samplings are then performed on the dimensional and dimensionless geometries, along with rotational speed and mass flow. The sampled parameters are subsequently converted into dimensionless groups, which are then utilized to train feed-forward neural networks. These networks form the basis of the surrogate models.

Hyperparameter tuning of surrogate models is a critical step in their development. To optimize the performance of the artificial neural networks (ANNs) used to model the various outputs, each ANN is trained via gradient descent within a genetic algorithm loop [17, 18]. The hyperparameters that govern the training process are chosen as decision variables to be optimized as presented in Table 1. Hyperparameter tuning can be computationally intensive, and we use a genetic algorithm with a total of 5 epochs and an initial population size of 100 to efficiently search the hyperparameter space. Two types of ANNs are trained: regressors, which predict continuous outputs such as the logarithmic decrement of the isentropic efficiency of the compressor, and classifiers, which predict categorical variables such as the stability of a given design or the functioning state of a compressor. The choice of loss function depends on the type of output being predicted and includes mean squared error or mean absolute error for regressors, and categorical cross-entropy for classifiers. Classifiers are trained with larger batch sizes than regressors.

To increase the accuracy and robustness of the surrogate model predictions, six different versions of the optimal artificial neural network (ANN) found via hyperparameter tuning with the genetic algorithm are trained using varying weight initializations. These initializations include He Normal, Lecun Normal, Glorot Uniform, He Uniform, Lecun Uniform, and Glorot Normal [19–21]. The final prediction is obtained as the average of the predictions from the six neural networks, resulting in an ensemble of neural networks [22].

2.3 Robustness

Robustness is a critical factor in engineering design, which can be defined in two ways. Firstly, robustness refers to the maxi-

mum space that a design can occupy without violating constraints due to manufacturing deviations. Secondly, a robust design can maintain its performance under manufacturing deviations, indicating its insensitivity to such deviations. These definitions have been formalized by Massoudi and Schiffmann [5] and are included in multi-objective optimization for robust design. In such optimization, the objectives are to maximize the feasible region (HV) and maximize the signal-to-noise ratio (S/N), among other competing objectives.

To estimate the maximum feasible space within manufacturing tolerances, a Monte Carlo method can be employed by randomly sampling points within the tolerances and identifying those that meet the constraints. The resulting feasible space (HV) can then be calculated by dividing the number of points that satisfy the constraints by the total number of sampled points. However, this method can be computationally expensive when dealing with high-dimensional design spaces. To increase efficiency, linear interpolation on a regular sampling grid can be used to generate additional points within the feasible space, thereby reducing the number of samples needed for accurate estimation without sacrificing computational power.

The signal-to-noise ratio (S/N) is another important metric used to measure the decline in performance metrics such as stability, load capacity, or efficiency across the feasible region defined by HV . In order to optimize the performance metric f , Equation (7) is used to maximize it, while Equation (8) is used to minimize it. The terms μ and σ^2 represent the mean and variance, respectively, and since S/N is always maximized in optimization, these two definitions ensure that μ is either maximized or minimized, while σ^2 is minimized. As an optimization objective, we employ the average (S/N) of the signal-to-noise ratio for stability, losses, and load capacity of the HGJB and SGTB.

$$S/N_f = 10 \cdot \log_{10} \left(\frac{\mu_f^2}{\sigma_f^2} \right) \quad (7)$$

$$S/N_f = -10 \cdot \log_{10} \left(\mu_f^2 + \sigma_f^2 \right) \quad (8)$$

Maximizing the signal-to-noise ratio (S/N) enables the optimization of performance metrics while controlling their gradients. When combined with the maximization of HV , it leads to a large feasible region with minimized gradients of the performance metrics.

2.4 Constrained Multi-Objective Optimization

Design optimization must consider a range of objectives and constraints to achieve a feasible and optimal solution. It is insufficient to optimize subsystems independently, as the interactions and interdependencies between subsystems must be accounted for. For the design of an electrically-driven compressor system supported by gas bearings, this means optimizing all subsystems simultaneously while meeting system requirements.

Specifically, the electric motor must deliver sufficient power to drive the impeller to the desired pressure ratio for a given mass flow rate, while the axial and radial bearings must be designed to support the impeller wheel's axial load and lift off the rotor, respectively. To ensure a stable design, rotordynamics and axial

TABLE 1: DESCRIPTION OF THE HYPERPARAMETERS SEARCHED FOR THE OPTIMIZATION OF THE FEED-FORWARD NEURAL NETWORKS.

Term	Symbol	Value
Number of neurons per hidden layer	n	16, 32, 64, 128, 256
Number of hidden layers	l	2, 3, 4
Activation	a	relu, selu, tanh, softplus, softsign
Optimiser	opt	Adam, Adamax, Adadelata, Adagrad
Batch size	bs	$2^{12}, 2^{13}, 2^{14}, 2^{15}/2^9, 2^{10}, 2^{11}, 2^{12}, 2^{13}, 2^{14}$
Kernel initialiser	ki	Glorot Normal (gn), He Normal (hn), Lecun Normal (ln), Glorot Uniform (gu), He Uniform (hu), Lecun Uniform (lu)
L2 penalisation	β_{L2}	$10^{-6}, 10^{-5}, 10^{-4}, 10^{-3}, 10^{-2}$
Learning rate	α_{lr}	0.01, 0.01, 0.1
Decay steps	ds	$10^3, 10^4, 10^5$

dynamics must be taken into consideration, with the rotor also satisfying bending frequency requirements to prevent destruction by resonance. Structural integrity must also be addressed by imposing constraints on the equivalent von Mises stress. Furthermore, the torque transmission between the rotor shaft and the magnet, as well as between the plug and the rotor shaft, are critical considerations.

3. METHODS

3.1 Impeller Wheel Representation

The turbocompressor sections are represented by multi-layer hollow cylinders to enable fast computation of the mass and moments of inertia of the entire turbocompressor unit, incorporating radial and axial bearings, shaft sections, and the electric motor. However, to accurately represent the impeller and its blades, a slicing method is required. The hub can be modeled as a stack of cylinders with varying radii. To extract mass and moments of inertia, a mapping from the 1D representation to a 3D representation of the impeller wheel must be defined. The meridional geometry of the hub and blades is defined by three ellipses, one arc of a circle, and the golden ratio ϕ , as shown in Fig 2. The hub and blades are parametrized by piecewise functions, presented in Eq. (10) and Eq. (11), respectively.

Neglecting the impeller blades can lead to significant deviations in the system's mass (m), polar moment of inertia (I_p), and transverse moment of inertia (I_t). As the impeller is rigidly attached at one end of the shaft in the studied rotor configurations, its contribution to the overall system stability cannot be underestimated. To account for this, the impeller and its blades are modeled as hollow cylinders, while maintaining the mass m and transverse moment of inertia I_t . The inner radius of the cylinders is set equal to the outer radius of the impeller hub, and their outer radius R_{cyl} and density ρ_{cyl} are determined by solving a system of two equations and two unknowns for each cylinder section, as presented in in Eq. (12) and Eq. (13).

To obtain a representation of the blades as equivalent hollow cylinders, rectangular prisms are used to bound the meridional hub and blade geometries. The splitters are accounted for by doubling the number of blades and spanning the full blade length, which provides the most conservative approximation as it increases the transverse moment of inertia of the whole im-

PELLER. This approximation is particularly relevant for stability computations. The blades and splitters are assumed to have equal thickness and are evenly distributed around the circumference of the hub to obtain the transverse moment of inertia. The moments of inertia of the rectangular prism about its principal axes are then transformed using a rotation matrix for each blade and respective angle θ , as computed in Eq. (14).

The transverse moment of inertia of each blade with respect to its angular position θ is computed using the parallel-axis theorem and can be found in Eq. (15), with the mass of each blade calculated using Eq. (16). The number of blades N_{bld} and the number of splitters N_{spl} determine the angular separation $\Delta\theta$ between each splitter and blade, which is given in Eq. (17). The moment of inertia of the n^{th} blade or splitter section spanning around the hub can be computed using Eq. (18). To obtain an equivalent hollow cylinder section, the total transverse moment of inertia I_t is calculated by summing the transverse moments of inertia of each blade and splitter section, and the same procedure is used for mass. Finally, the outer radius R_{cyl} and density ρ_{cyl} of each cylinder section are determined by solving the system of two equations and two unknowns using Eq. (12) and Eq. (13).

3.2 Design Rules

To enable the optimization process for the entire turbocompressor unit, it is necessary to establish design rules. The first rule concerns the positioning of the five subsystems in a single-stage electrically driven turbocompressor for heat pump applications with gas bearings, namely the compressor (C), axial bearing (S), radial bearings A and B, and electric motor (E). As there are five subsystems, there are $5! = 120$ permutations. However, as radial bearings A and B are identical, they are insensitive to permutation. To minimize axial deviation of the impeller due to thermal expansion of the rotor shaft during operation, the spiral groove thrust bearing is placed next to the impeller. Therefore, the impeller wheel can only be located at one of the two free ends of the rotor shaft, followed directly by the axial bearing. Any other placement of the impeller would impose difficult constraints in assembly, manufacturing, aerodynamic performance, and placing of the volute. This leaves only two permitted permutations for consideration in the optimization: 'CSABE' or 'CSAEB', where the electric motor is either at the other free end or placed be-

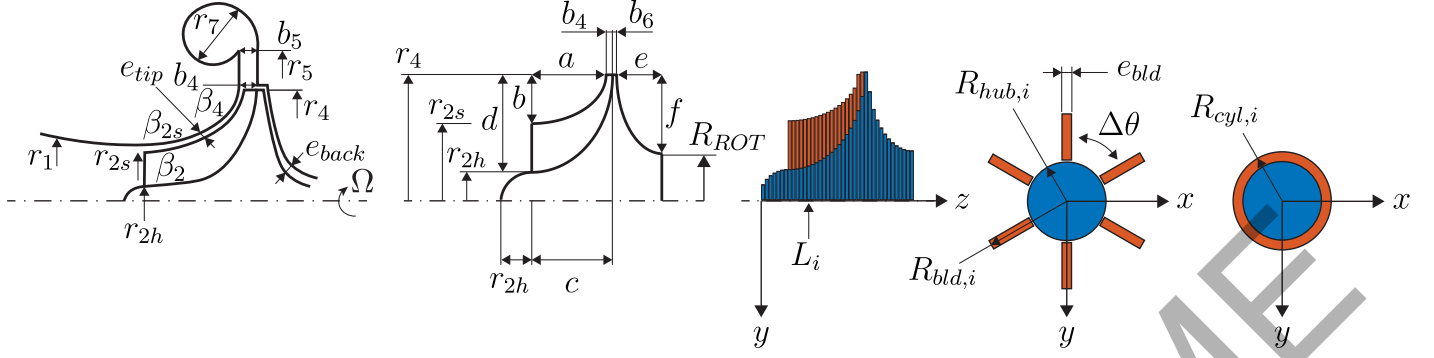


FIGURE 2: SCHEMATIC REPRESENTATION OF THE IMPELLER WHEEL TRANSFORMATION TO A 2-LAYER CYLINDER MODEL. THE MERIDIONAL GEOMETRY OF THE HUB AND BLADES ARE DEFINED BY THREE ELLIPSES, ONE ARC OF A CIRCLE, AND THE GOLDEN RATIO ϕ . THE HUB AND BLADE GEOMETRIES ARE PARAMETRIZED USING PIECEWISE FUNCTIONS. THE TRANSFORMATION FROM THE IMPELLER TO THE FULL 2-LAYER CYLINDER REPRESENTATION IS PERFORMED USING THE FUNCTIONS DEFINED IN THE ANNEX.

tween the radial bearings to bring the center of gravity between both bearings. After eliminating the permutations resulting from pure symmetry, this study focuses on the 'CSABE' layout, with the compressor on the left end and the electric motor on the right end, as shown in Fig. 3. The optimization process involves various geometrical variables, and the front and unrolled views of the SGTB and HGJB are presented. The impeller wheel is made of metal, such as stainless steel or aluminum, while the plug connecting the impeller and the rotor is made of inconel, a Nickel-based alloy. The rotor shaft, which can be hollow, has the same outer radius R_{ROT} throughout its length, including the radial bearings. The magnet, made of neodymium or samarium-cobalt, is inserted into the shaft by interference. The type of metal, hard metal or magnet used is also an optimization decision variable.

3.3 Constrained Multi-Objective Optimization Setup

The optimization process employed in this study utilized the Non-dominated Sorting Genetic Algorithm III (NSGA-III) [23, 24], which is a widely used evolutionary algorithm for multi-objective optimization. The algorithm was implemented using Python [25]. To enhance the efficiency of the optimization process, an adaptive-operator selection procedure was utilized. This procedure adapts the selection of genetic operators to the problem's characteristics, as proposed by Vrugt and Robinson [26] and Hádka and Reed [27]. Additionally, to guide the optimization process, a set of uniformly sampled reference directions was used, which was proposed by Das and Dennis [28]. The optimization process was run for 50 generations.

The optimization process focuses on four key objectives, as outlined in Table 2. Firstly, the objective is to maximize the geometric mean of the feasible regions, represented by \overline{HV} , for both the radial bearings and the axial bearing. This objective accounts for manufacturing deviations. Secondly, the objective is to maximize HV_{COMP} , which ensures the attainment of the largest

compressor maps. To further evaluate the performance, the mean signal-to-noise ratio of the radial bearings ($\overline{S/N}_{HGJB}$) is computed by considering the average of the signal-to-noise ratios associated with load capacity, logarithmic decrement (stability), and losses. Similarly, the mean signal-to-noise ratio of the axial bearing ($\overline{S/N}_{SGTB}$) is determined. Additionally, the signal-to-noise ratio of the isentropic efficiency of the compressor ($\overline{S/N}_{\eta_{is,COMP}}$) is considered. The third objective aims to maximize the harmonic mean of $\overline{S/N}_{HGJB}$, $\overline{S/N}_{SGTB}$, and $\overline{S/N}_{\eta_{is,COMP}}$, which provides an overall assessment of the signal-to-noise ratios with respect to manufacturing deviations and the range of operating conditions. Lastly, the overall efficiency of the machine, denoted as η_{tot} , is maximized. η_{tot} is defined as the ratio of the isentropic power work of the compressor ($\dot{E}_{is,COMP}$) to the sum of its mechanical power work ($\dot{E}_{COMP} = \dot{E}_{is,COMP}/\eta_{is,COMP}$), losses in the two radial bearings (\dot{E}_{HGJB}), losses in the axial bearing (\dot{E}_{SGTB}), and windage loss of the electric motor ($\dot{E}_{EM,loss}$). These four objectives collectively drive the optimization process and contribute to enhancing the performance and efficiency of the turbocompressor system.

$$\eta_{tot} = \frac{\dot{E}_{is,COMP}}{\frac{\dot{E}_{is,COMP}}{\eta_{is,COMP}} + 2\dot{E}_{HGJB} + \dot{E}_{SGTB} + \dot{E}_{EM,loss}} \quad (9)$$

TABLE 2: OBJECTIVES OF THE MULTI-OBJECTIVE OPTIMIZATION

Term	Symbol	Objective type	Unit
<i>Objectives</i>			
Geometric mean of bearings feasible regions	\overline{HV}	Maximize	μm
Feasible region compressor	HV_{COMP}	Maximize	RPM kg s^{-1}
Harmonic mean of the signal-to-noise ratios	$\overline{S/N}$	Maximize	—
System efficiency	η_{tot}	Maximize	—

The optimization problem incorporates several constraints

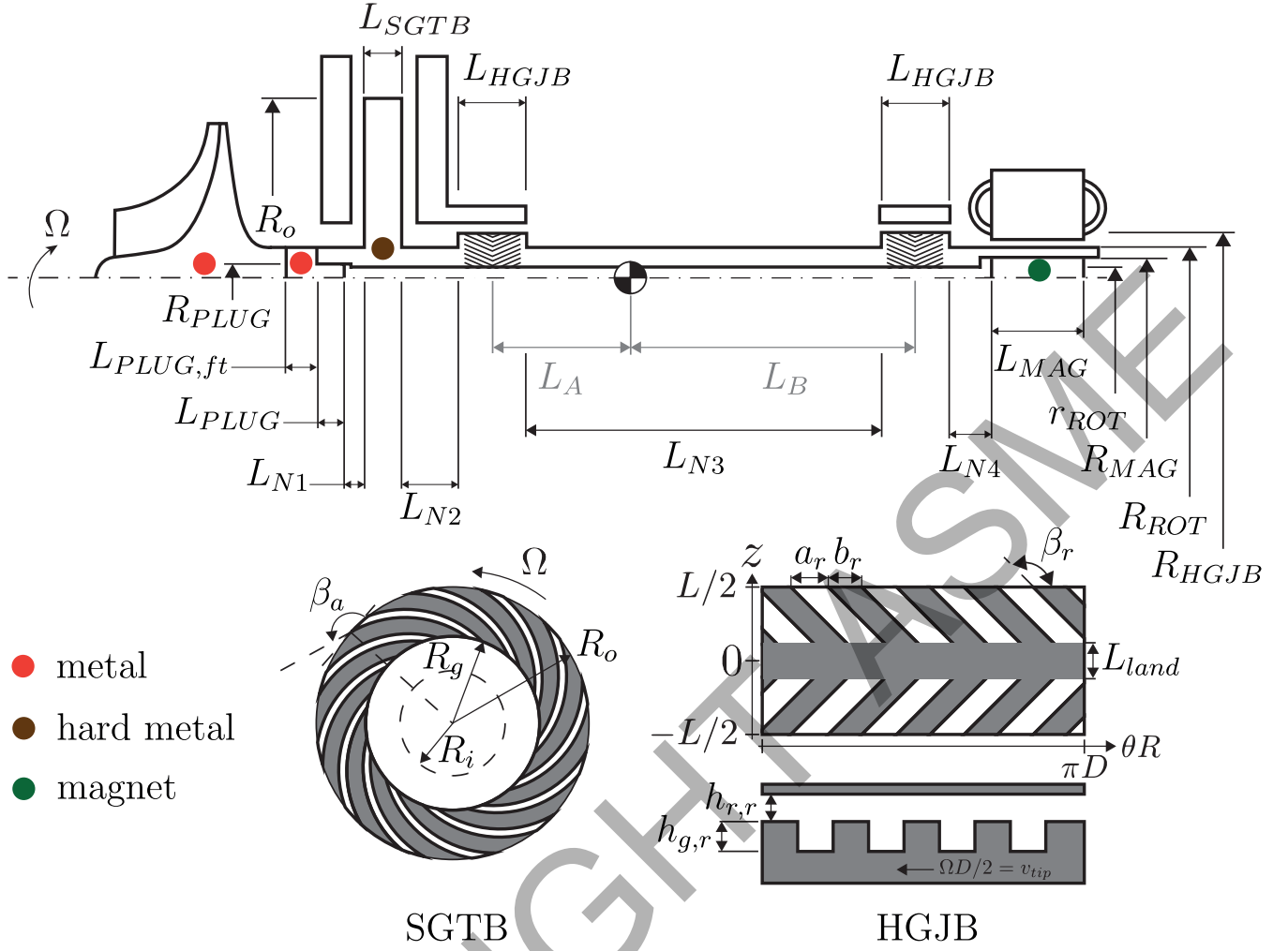


FIGURE 3: THE COMPLETE TURBOCOMPRESSOR UNIT WITH ALL GEOMETRIC VARIABLES USED IN OPTIMIZATION, INCLUDING LENGTHS AND RADII, AND MATERIALS SPECIFIED. THE SCHEMATIC DIAGRAMS OF THE SPIRAL GROOVE THRUST BEARINGS (SGTB) AND HERRINGBONE GROOVED JOURNAL BEARINGS (HGJB) ARE SHOWN WITH THEIR RESPECTIVE VARIABLES. THE LAYOUT OF THE SUBSYSTEMS FOLLOWS THE 'CSABE' PERMUTATION.

to ensure the feasibility and reliability of the designed turbocompressor system, as summarized in Table 3. First, a load capacity condition is enforced to ensure rotor lift-off with a safety margin of 20% at a rotor speed of 10,000 rpm. The radial expansion is limited to a maximum of 2 micrometers to allow for designs with low nominal bearing clearance, while ensuring mechanical stability. A position constraint is also imposed on the radial bearings relative to the center of gravity (CG) of the system, requiring that their dot product be negative to ensure they are located on opposite sides of the CG. Additionally, stable designs are chosen with a safety margin of 0.1 on the logarithmic decrement of the rotordynamics of the radial bearings (Γ_{HGJB}) and the driven dynamics of the axial bearing (Γ_{SGTB}). The compressibility numbers (Λ_{HGJB} and Λ_{SGTB}) must remain below 60 and 120, respectively, to ensure that the optimization stays within the range of the training data used in the surrogate models. To account for manufacturing deviations in bearings, at least 30% of the sampled region must satisfy the constraints. A minimum sampling rate of 1%

is set for the compressor map to ensure feasible designs. Constraints are also applied to the excitation frequency to ensure that the cylindrical forward excitation frequency is greater than the backward mode frequency for most points, and that it increases monotonically at a decreasing rate. The optimization process avoids designs that exhibit a specific type of Pareto optimum in which the cylindrical forward excitation frequency suddenly collapses to a subsynchronous mode. The center of gravity should not coincide with the bearings, and this is ensured by enforcing constraints on the distances of the CG from each radial bearing midplane ($\bar{L}_A > 0.5$ and $\bar{L}_B > 0.5$). Furthermore, constraints are applied on the equivalent von Mises stress to guarantee the structural integrity of the turbocompressor components, including the magnet, plug, and rotor. The electric motor must provide sufficient power to compensate for all losses and drive the compressor, while ensuring that interference between the magnet and shaft and between the plug and shaft provide enough friction to transmit torque. The von Mises stress must remain below half

the yield strength, taking into account various operating conditions. A similar safety factor is applied to the radial and axial bearings. Finally, the maximum pressure ratio observed in the compressor map is bounded to be at least 4, and a lower boundary of 0.1 is set on the compressor isentropic efficiency to ensure adequate performance. In order to mitigate the risk of rotor failure resulting from resonance, a conservative approach is taken by setting the maximum rotational speed to 83% of the bending frequency. This precautionary measure provides a significant safety margin, considering the small clearance observed at high speeds. By adhering to this limitation, the system ensures the integrity and durability of the rotor under operating conditions prone to resonance-induced catastrophic failures.

TABLE 3: CONSTRAINTS OF THE MULTI-OBJECTIVE OPTIMIZATION

Description	Constraint	Unit
Lift force	$F_{\text{HGJB}, 10 \text{ kRPM}} > 1.20 \cdot F_{\text{W}}$	N
Centrifugal growth	$\Delta h_{r,\text{exp}} < 2 \cdot 10^{-6}$	m
CG between bearings	$\mathbf{GA} \cdot \mathbf{GB} < 0$	m ²
HGJB stability	$\Gamma_{\text{HGJB}} > 0.1$	—
SGTB stability	$\Gamma_{\text{SGTB}} > 0.1$	—
HGJB compressibility number	$\Lambda_{\text{HGJB}} < 60$	—
SGTB compressibility number	$\Lambda_{\text{SGTB}} < 120$	—
HGJB feasible region	$HV_{\text{HGJB}} > 0.3$	—
SGTB feasible region	$HV_{\text{SGTB}} > 0.3$	—
Compressor feasible region	$HV_{\text{COMP}} > 0.01$	—
Cylindrical excitation modes	$\Omega_{\text{ex,cyl}_F} > \Omega_{\text{ex,cyl}_B}$	RPM
Cylindrical forward concavity	$\frac{\partial^2 \Omega_{\text{ex,cyl}_F}}{\partial N^2} < 0$	RPM ⁻¹
Cylindrical forward growth	$\frac{\partial \Omega_{\text{ex,cyl}_F}}{\partial N} > 0$	—
CG away from bearing A	$\bar{L}_A > 0.5$	—
CG away from bearing B	$\bar{L}_B > 0.5$	—
Plug-rotor interference	$\delta_{\text{PLUG}} > 0$	m
Plug torque transmission ratio	$S_{\tau,\text{PLUG}} > 1$	—
Plug von Mises safety factor	$S_{\sigma_{VM},\text{PLUG}} > 2$	—
Magnet-rotor interference	$\delta_{\text{MAG}} > 0$	m
Magnet torque transmission ratio	$S_{\tau,\text{MAG}} > 1$	—
Magnet von Mises safety factor	$S_{\sigma_{VM},\text{MAG}} > 2$	—
SGTB von Mises safety factor	$S_{\sigma_{VM},\text{SGTB}} > 2$	—
HGJB von Mises safety factor	$S_{\sigma_{VM},\text{HGJB}} > 2$	—
SGTB axial force	$F_{\text{SGTB}} > F_{\text{COMP}}$	N
Electric motor power	$\dot{E}_{\text{EM}} > \dot{E}_{\text{losses}} + \dot{E}_{\text{COMP}}$	W
Turbocompressor rotor length	$N_{\text{end}} < 1.20 \cdot 60 \cdot f_{\text{bend}}$	RPM
Compressor isentropic efficiency	$\eta_{\text{is,comp}} > 0.1$	—
Compressor pressure ratio	$\max(\Pi) > 4$	—

The decision variables for the multi-objective optimization are listed in Tab. 4 along with their respective ranges. The impeller wheel variables, which determine the wheel's characteristics, are open for optimization. Wheels with a maximum tip radius of $r_4 = 35 \text{ mm}$ are permitted. The inlet blade angles β_2 and β_{2s} are fixed, and the number of splitter blades is set equal to the number of blades. The operating conditions are also fixed at an inlet pressure of 2.51 bar and an inlet temperature of 300 K using R134a refrigerant. These conditions are applied to the bearings while considering the fluid viscosity. The two HGJBs are identical, so only one HGJB's geometry is optimized. The geometry of the SGTB is also used as an input to the optimizer. The rotor geometry is bounded by the inner radius r_{ROT} and the

outer radius R_{ROT} . The pockets that hold the plug and magnet have radii R_{PLUG} and R_{MAG} with respective interference δ_{PLUG} and δ_{MAG} . Lengths and radii are defined as ratios with respect to R_{ROT} . Materials are defined as float values between 0 and 1 and are mapped to integers to select all different types of metals for the compressor, hard metal for the rotor, and magnet. To ensure robustness of the bearings, the optimizer selects the feasible range for the deviations of local bearing clearance and groove depth, within which the largest possible deviations are chosen subject to constraints ensuring functional and operational requirements. The sampling method is fixed as a linspace, with the boundaries of the linspace changing with the selected deviation range. The choice of deviation range balances the need for robustness with the need for sufficient sampling to detect feasible regions in the design. Seven points are used to sweep each variable for manufacturing deviations. Due to the compressor map's consideration, a sampling of 13 points is made for the rotational speed, and 13 points are swept for the mass flow.

4. RESULTS

The results of the multi-objective optimization are presented in the form of pairplots, as depicted in Figure 4. The solution with the largest geometric mean of the bearings feasible regions (\overline{HV}) is indicated by a red dot on the scatter plots. The optimization process involved a search of 1716 nominal designs over 500 generations, resulting in a total of 1.2 billions samples. The optimization was completed within approximately 1 day using a desktop computer equipped with a 12-core AMD Ryzen 3900X CPU and a Nvidia RTX 3090 GPU.

The pairplots shown in Fig. 4 illustrate the trade-off between robustness against manufacturing deviations (\overline{HV}) and robustness against variance in the performance metric ($\overline{S/N}$) which are negatively correlated. The diagonal of the pairplots displays the distribution of each objective over the range covered. On average, the geometric mean of the feasible region of the radial and axial bearings is of $20 \mu\text{m}^2$. \overline{HV} and HV_{COMP} are negatively correlated to global efficiency (η_{tot}), highlighting the trade-offs involved in achieving robustness and an efficient design.

The turbocompressor that was selected for the study is presented in Figure 5, whereby its axial and radial dimensions are expressed in millimeters. The figure displays the turbocompressor map and response surfaces in the form of contour plots for the axial dynamics (Γ_{SGTB}) and rotordynamics (Γ_{HGJB}) against manufacturing deviations, with white lines indicating evaluations conducted using baseline models to monitor the accuracy of the surrogate models in predicting system dynamics. Notably, the rotordynamics is predicted accurately, with slight overprediction observed for the axial dynamics. The study findings indicate that local bearing clearance and groove depth deviations, of $\pm 5 \mu\text{m}$ and $\pm 1.5 \mu\text{m}$, can be safely achieved respectively for the axial bearing and radial bearings. The optimized turbocompressor rotor has a mass of 412 g and midplane bearing distances to the center of gravity of $L_A = 28.8 \text{ mm}$ and $L_B = 22.1 \text{ mm}$. The length-to-diameter aspect ratio of the HGJB is of $LoD = 1.4$. The impeller wheel is composed of aluminum, while the magnet and rotor are made of neodymium and tungsten carbide, respectively. Finally, the study results reveal that a pressure ratio of 4

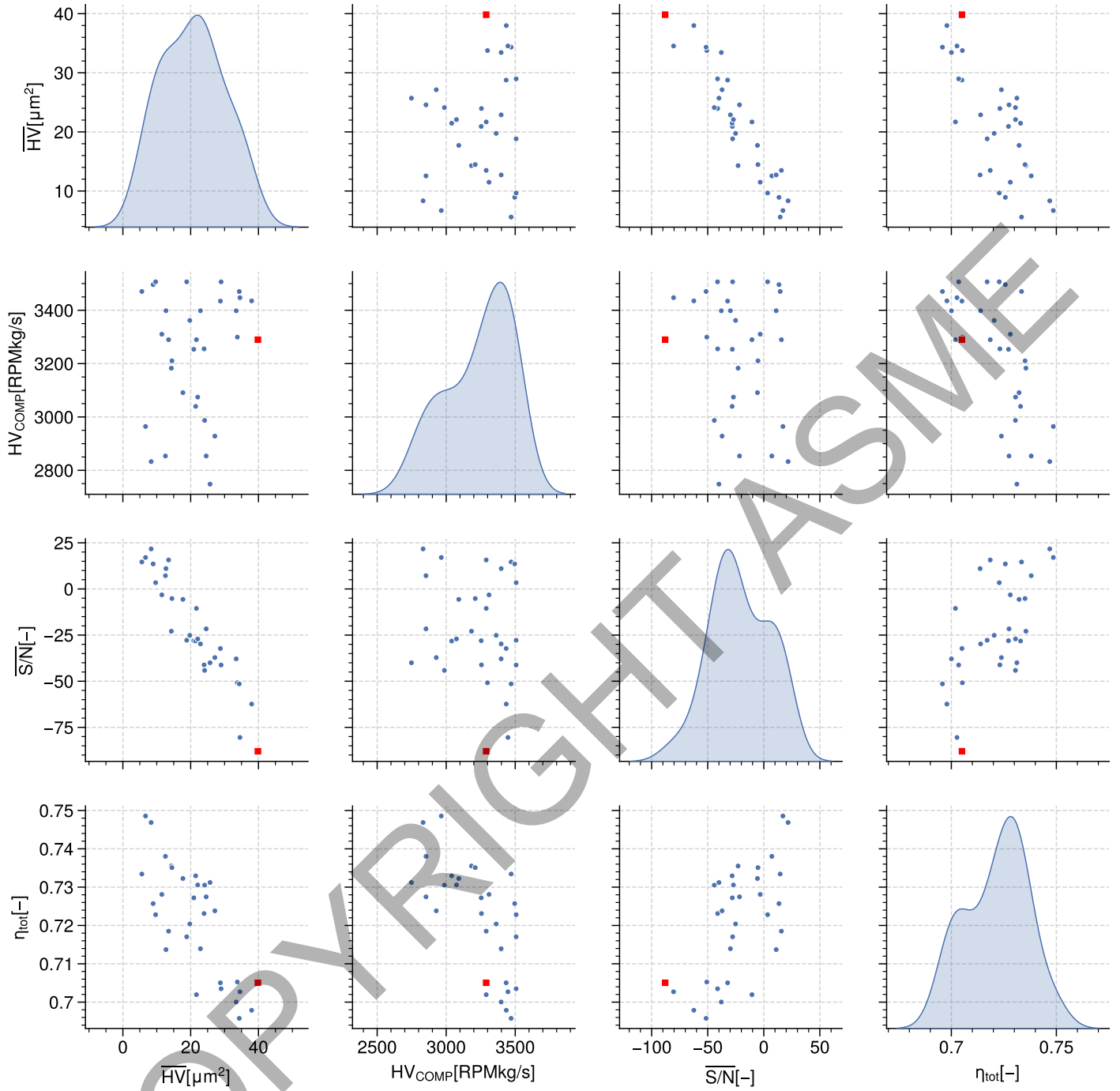


FIGURE 4: PARETO FRONT OF FOUR OBJECTIVES FROM TURBOCOMPRESSOR OPTIMIZATION PRESENTED AS PAIRPLOTS WITH SELECTED SOLUTION (RED DOT) FOR LARGEST GEOMETRIC MEAN OF THE FEASIBLE REGION OF THE BEARINGS (\overline{HV}). DIAGONAL SHOWS OBJECTIVE DISTRIBUTION.

is reached for $N_{\text{end}} = 162\,737$ RPM which is much lower than the bending frequency of $N_{\text{bend}} = 216\,532$ RPM. The compressor can operate with an isentropic efficiency higher than 0.8 over a large portion of the compressor map, for speeds ranging from 50 kRPM to 163 kRPM, for a consumed compressor power ranging from 300 W to 3000 W.

5. DISCUSSION

The competition between robustness metric \overline{HV} and $\overline{S/N}$ are consistent with those reported in previous studies. Massoudi and Schiffmann [6] also found that increasing the feasible region leads to a trade-off between robustness with respect to constraints and robustness with respect to signal-to-noise ratio. The larger

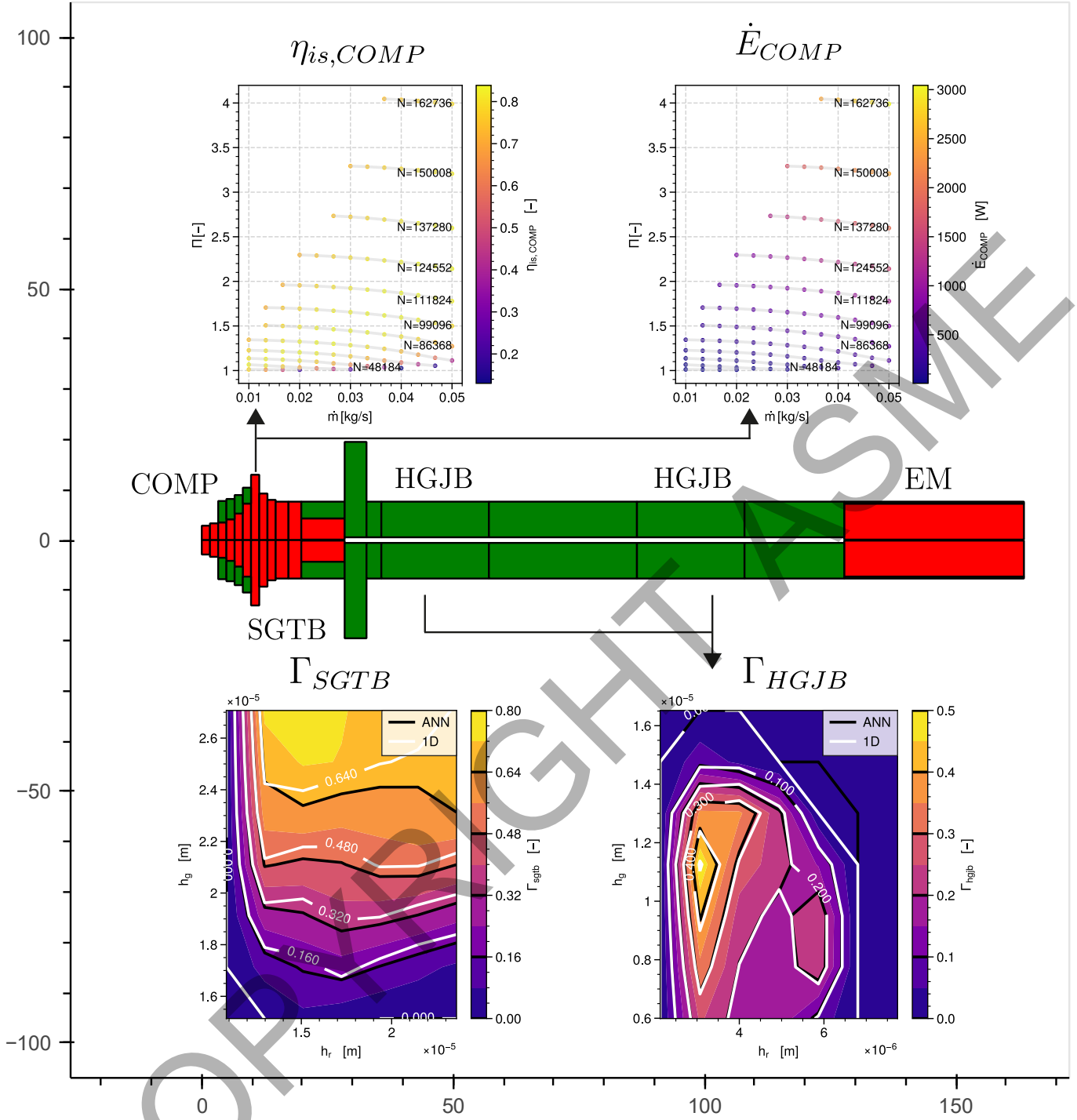


FIGURE 5: THE SELECTED TURBOCOMPRESSOR DESIGN WITH MIDPLANE BEARING DISTANCES OF $L_A = 28.8$ mm AND $L_B = 22.1$ mm, HGJB LENGTH TO DIAMETER ASPECT RATIO OF 1.4 AND A MASS OF 412 g.

the feasible region, the more difficult indeed to maintain a given performance metric constant.

The selected solution, aiming to maximize the feasible region of the bearings, demonstrates a radial bearing length-to-diameter aspect ratio (LoD) close to 1.4. Notably, the midplane distances from the bearings to the center of gravity, although not entirely equal, are found to be in close proximity. The observed discrepancy can be attributed to the selection of aluminum as

the impeller material. Although this choice reduces the overall weight of the turbocompressor, the inclusion of the necessary magnet on the opposite end of the shaft shifts the center of gravity towards the right. In order to address this, an extension in the shaft length could potentially shift the center of gravity towards the left. However, such a modification would inevitably result in a decrease in bending frequency. These findings align with Massoudi and Schiffmann's recent study on the robustness of gas

TABLE 4: DESCRIPTION OF THE PARAMETERS FOR THE MULTI-OBJECTIVE OPTIMIZATION

Term	Symbol	Range/Value	Unit
<i>Impeller Variables</i>			
Tip radius	r_4	$7 \cdot 10^{-3} - 35 \cdot 10^{-3}$	m
Inducer hub radius ratio	r_{2h}/r_4	0.1 – 0.3	–
Inlet shroud radius ratio	r_{2s}/r_{2h}	1.2 – 2.3	–
Inducer inlet radius ratio	r_1/r_{2s}	1.05 – 1.3	–
Diffuser exit radius ratio	r_5/r_4	1.05 – 1.5	–
Tip width ratio	b_4/r_4	0.015 – 0.3	–
Tip clearance ratio	e_{tip}/b_4	0.01 – 0.015	–
Backface clearance ratio	e_{back}/r_4	0.001 – 0.15	–
Inducer length ratio	L_{ind}/r_4	1.05 – 4	–
Exit blade angle	β_4	–45 – 0	°
Blade thickness	e_{bid}	$0.1 - 0.5 \cdot 10^{-3}$	m
Number of blades	N_{bid}	5 – 11	–
<i>HGJB Variables</i>			
Groove width ratio	α_r	0.32–0.68	–
Groove angle	β_r	–167.5 – –122.5	°
Grooved land region ratio	γ_r	0.52 – 0.97	–
Groove depth	$h_{g,r}$	$2.5 \cdot 10^{-6} - 28.5 \cdot 10^{-6}$	m
Local bearing clearance	$h_{r,r}$	$2.5 \cdot 10^{-6} - 28.5 \cdot 10^{-6}$	m
$h_{g,r}$ deviations	$\Delta h_{g,r}$	$1 \cdot 10^{-6} - 10 \cdot 10^{-6}$	m
$h_{r,r}$ deviations	$\Delta h_{r,r}$	$1 \cdot 10^{-6} - 10 \cdot 10^{-6}$	m
<i>SGTB Variables</i>			
Groove width ratio	α_a	0.32–0.68	–
Groove angle	β_a	–167.5 – –122.5	°
Grooved land region ratio	γ_a	0.1 – 0.9	–
Groove depth	$h_{g,a}$	$2.5 \cdot 10^{-6} - 28.5 \cdot 10^{-6}$	m
Local bearing clearance	$h_{r,a}$	$2.5 \cdot 10^{-6} - 28.5 \cdot 10^{-6}$	m
$h_{g,a}$ deviations	$\Delta h_{g,a}$	$1 \cdot 10^{-6} - 10 \cdot 10^{-6}$	m
$h_{r,a}$ deviations	$\Delta h_{r,a}$	$1 \cdot 10^{-6} - 10 \cdot 10^{-6}$	m
<i>Rotor Variables</i>			
Rotor outer radius	R_{ROT}	$5 \cdot 10^{-3} - 30 \cdot 10^{-3}$	m
Rotor inner radius ratio	r_{ROT}/R_{ROT}	$0 - 0.95 \cdot 10^{-3}$	–
Plug radius ratio	R_{PLUG}/R_{ROT}	0.3 – 0.95	–
SGTB radius ratio	R_o/R_{ROT}	1.15 – 10	–
Magnet radius ratio	R_{MAG}/R_{ROT}	0.3 – 0.95	–
Segment 1 length ratio	L_{N1}/R_{ROT}	0.3 – 12	–
Segment 2 length ratio	L_{N2}/R_{ROT}	0.3 – 12	–
Segment 3 length ratio	L_{N3}/R_{ROT}	0.3 – 12	–
Segment 4 length ratio	L_{N4}/R_{ROT}	0.3 – 12	–
SGTB length ratio	L_{SGTB}/R_o	2/7 – 5/9	–
HGJB length ratio	L_{HGJB}/R_{ROT}	1 – 4	–
Magnet length ratio	L_{MAG}/R_{ROT}	1 – 12	–
Nominal rotor-plug interference	δ_{PLUG}	$1 \cdot 10^{-6} - 100 \cdot 10^{-6}$	m
Nominal rotor-magnet interference	δ_{MAG}	$1 \cdot 10^{-6} - 100 \cdot 10^{-6}$	m
<i>Material Variables</i>			
Impeller wheel material	Mat_{COMP}	0 – 1	–
Rotor material	Mat_{ROT}	0 – 1	–
Magnet material	Mat_{MAG}	0 – 1	–
<i>Operating Variables</i>			
Maximum rotor speed	N_{end}	$1.5 \cdot 10^5 - 5 \cdot 10^5$	RPM
<i>Dependent parameters</i>			
HGJB radius	R_{HGJB}	R_{ROT}	m
Front plug length	$L_{PLUG,ft}$	$1/3 \cdot R_{ROT}$	m
Number of splitter blades	N_{splits}	N_{bid}	–
<i>Fixed parameters</i>			
Startup rotor speed	N_{start}	$2 \cdot 10^4$	RPM
Robustness sampling unit	k_{rob}	7	–
Speed sampling sweep	k_N	13	–
Mass flow sweep	k_{in}	13	–
Fluid	R134a		
Compressor inlet pressure	P_{in}	$2.51 \cdot 10^5$	Pa
Compressor inlet temperature	T_{in}	300	K
Mass flow lower bound	\dot{m}_{start}	10	g s ⁻¹
Mass flow upper bound	\dot{m}_{end}	50	g s ⁻¹
Compressor inlet blade angle at hub	β_2	–56	°
Compressor inlet blade angle at shroud	β_{2s}	–60	°

bearing supported rotors [5]. Their research suggests that a symmetrical design, or a design with a large LoD , offers enhanced robustness against manufacturing deviations in radial bearings. In the pursuit of higher system efficiency, this optimization has

led to a reduction in LoD to minimize losses through a shorter bearing length.

The maximization of compressor isentropic efficiency is an integral aspect of optimizing the overall efficiency, denoted as η_{tot} . Notably, the isentropic efficiency exhibits a consistently high value, reaching 0.8 across a significant portion of the compressor map. This observation aligns with Schiffmann and Favrat’s comprehensive study on optimal compressor designs for both single and multiple operating points [12]. Their study suggests that the best efficiency is achieved at the nominal speed of $N_{nom} = 130$ kRPM for a first stage pressure ratio of $\Pi = 2.4$. In accordance with their findings, the operating point selected for this study corresponds to their A2 operating point.

6. CONCLUSION

This study has introduced an automated framework for the integrated design of gas bearings supported turbocompressors while considering manufacturing deviations. This was made possible by the use of constrained multi-objective optimization and surrogate models made of ensembles of feed-forward neural networks. This allowed us to bypass the traditional sequential approach, integrating the optimization of all subsystems in one loop. The results clearly indicate the gain in computational time for such an approach and clearly demonstrate its strength compared to a traditional integrated nominal optimization. To the best of our knowledge, it is the first time the design of such a system has been done by considering both the integration and the robustness.

Future work will focus on the variation of the selection of different rotor layouts and subsystems configurations. Furthermore, this methodology can be extended to other fields in engineering that require the integration of multiple subsystems and consideration of robustness against manufacturing deviations. The presented framework highlights the importance of a comprehensive and integrated approach to system design and provides a valuable foundation for future research in this area.

ACKNOWLEDGMENTS

The authors acknowledge the MIT SuperCloud and Lincoln Laboratory Supercomputing Center for providing high-power computing resources that have contributed to the research results reported within this paper.

REFERENCES

- [1] Wehner, M., Truby, R. L., Fitzgerald, D. J., Mosadegh, B., Whitesides, G. M., Lewis, J. A. and Wood, R. J. “An Integrated Design and Fabrication Strategy for Entirely Soft, Autonomous Robots.” *nature* Vol. 536 No. 7617 (2016): pp. 451–455. DOI [10.1038/nature19100](https://doi.org/10.1038/nature19100).
- [2] Picard, C. and Schiffmann, J. “Automated design tool for automotive control actuators.” *International Design Engineering Technical Conferences and Computers and Information in Engineering Conference*, Vol. 84010: p. V11BT11A027. 2020. American Society of Mechanical Engineers. DOI [10.1115/DETC2020-22390](https://doi.org/10.1115/DETC2020-22390).
- [3] Schiffmann, J. “Integrated design and multi-objective optimization of a single stage heat-pump turbocompressor.”

- Journal of Turbomachinery* Vol. 137 No. 7 (2015): p. 071002. DOI [10.1115/1.4029123](https://doi.org/10.1115/1.4029123).
- [4] Guenat, E. and Schiffmann, J. "Multi-Objective Optimization of Grooved Gas Journal Bearings for Robustness in Manufacturing Tolerances." *Tribology Transactions* Vol. 62 No. 6 (2019): pp. 1041–1050. DOI [10.1080/10402004.2019.1642547](https://doi.org/10.1080/10402004.2019.1642547).
 - [5] Massoudi, S. and Schiffmann, J. "Robust Design of Herringbone Grooved Journal Bearings using Multi-Objective Optimization assisted with Artificial Neural Networks." *Turbomachinery Technical Conference and Exposition*, Vol. 18. 2023. American Society of Mechanical Engineers.
 - [6] Massoudi, S. and Schiffmann, J. "Ensemble Neural Network Modeling of Gas Bearings Supported Rotors: A Global Surrogate Approach in Multi-Objective Optimization for Robust Design." 2023.
 - [7] Vohr, J. H. and Chow, C. Y. "Characteristics of Herringbone-Grooved, Gas-Lubricated Journal Bearings." *Journal of Basic Engineering* Vol. 87 No. 3 (1965): pp. 568–576. DOI [10.1115/1.3650607](https://doi.org/10.1115/1.3650607).
 - [8] Nelson, H. D. and McVaugh, J. M. "The Dynamics of Rotor-Bearing Systems Using Finite Elements." *Journal of Engineering for Industry* Vol. 98 No. 2 (1976): pp. 593–600. DOI [10.1115/1.3438942](https://doi.org/10.1115/1.3438942).
 - [9] Nelson, H. D. "A Finite Rotating Shaft Element Using Timoshenko Beam Theory." *Journal of Mechanical Design* Vol. 102 No. 4 (1980): pp. 793–803. DOI [10.1115/1.3254824](https://doi.org/10.1115/1.3254824).
 - [10] Lepe, F., Mora, D. and Rodríguez, R. "Locking-free finite element method for a bending moment formulation of Timoshenko beams." *Computers & Mathematics with Applications* Vol. 68 No. 3 (2014): pp. 118–131. DOI [10.1016/j.camwa.2014.05.011](https://doi.org/10.1016/j.camwa.2014.05.011).
 - [11] Picard, C., Schiffmann, J. and A., Faez. "DATED: Guidelines for Creating Synthetic Datasets for Engineering Design Applications." *International Design Engineering Technical Conferences and Computers and Information in Engineering Conference*. 2023. American Society of Mechanical Engineers. DOI [10.1115/DETC2023-111609](https://doi.org/10.1115/DETC2023-111609).
 - [12] Schiffmann, J. and Favrat, D. "Design, experimental investigation and multi-objective optimization of a small-scale radial compressor for heat pump applications." *Energy* Vol. 35 No. 1 (2010): pp. 436–450. DOI [10.1016/j.energy.2009.10.010](https://doi.org/10.1016/j.energy.2009.10.010). Accessed 2021-05-07, URL <https://www.sciencedirect.com/science/article/pii/S0360544209004435>.
 - [13] Miller, Timothy John Eastham. *Switched reluctance motors and their control*. Magna physics publishing and clarendon press (1993).
 - [14] Rosset, K. and Schiffmann, J. "Extended Windage Loss Models for Gas Bearing Supported Spindles Operated in Dense Gases." *Journal of Engineering for Gas Turbines and Power* Vol. 142 No. 6 (2020). DOI [10.1115/1.4047124](https://doi.org/10.1115/1.4047124). Accessed 2023-03-13, URL <https://doi.org/10.1115/1.4047124>.
 - [15] Guenat, E. and Schiffmann, J. "Effects of humid air on aerodynamic journal bearings." *Tribology International* Vol. 127 (2018): pp. 333–340. DOI [10.1016/j.triboint.2018.06.002](https://doi.org/10.1016/j.triboint.2018.06.002). Accessed 2020-04-27, URL <http://www.sciencedirect.com/science/article/pii/S0301679X18302883>.
 - [16] Olmedo, L. E. and Schiffmann, J. "Towards a real-time capable hybrid-twin for gas-bearing supported high-speed turbocompressors." *Energy* Vol. 275 (2023): p. 127385. DOI [10.1016/j.energy.2023.127385](https://doi.org/10.1016/j.energy.2023.127385). Accessed 2023-05-15, URL <https://www.sciencedirect.com/science/article/pii/S036054422300779X>.
 - [17] Massoudi, S., Picard, C. and Schiffmann, J. "Robust Design Using Multiobjective Optimisation and Artificial Neural Networks with Application to a Heat Pump Radial Compressor." *Design Science* Vol. 8 (2022): pp. 1041–1050. DOI [10.1017/dsj.2021.25](https://doi.org/10.1017/dsj.2021.25).
 - [18] Papavasileiou, E., Cornelis, J. and Jansen, B. "A Systematic Literature Review of the Successors of "NeuroEvolution of Augmenting Topologies"." *Evolutionary Computation* Vol. 29 No. 1 (2021): pp. 1–73. DOI [10.1162/evco_a_00282](https://doi.org/10.1162/evco_a_00282).
 - [19] He, K., Zhang, X., Ren, S. and Sun, J. "Delving Deep into Rectifiers: Surpassing Human-Level Performance on ImageNet Classification." *2015 IEEE International Conference on Computer Vision (ICCV)*: pp. 1026–1034. 2015. DOI [10.1109/ICCV.2015.123](https://doi.org/10.1109/ICCV.2015.123).
 - [20] Glorot, X. and Bengio, Y. "Understanding the difficulty of training deep feedforward neural networks." *Proceedings of the thirteenth international conference on artificial intelligence and statistics*: pp. 249–256. 2010. JMLR Workshop and Conference Proceedings.
 - [21] LeCun, Y. A., Bottou, L., Orr, G. B. and M., Klaus-Robert. "Efficient backprop." *Neural networks: Tricks of the trade*. Springer (2012): pp. 9–48. DOI [10.1007/978-3-642-35289-8_3](https://doi.org/10.1007/978-3-642-35289-8_3).
 - [22] Ganaie, M. A., Hu, Minghui, Malik, A. K., Tanveer, M. and Suganthan, P. N. "Ensemble deep learning: A review." *Engineering Applications of Artificial Intelligence* Vol. 115 (2022). DOI [10.1016/j.engappai.2022.105151](https://doi.org/10.1016/j.engappai.2022.105151).
 - [23] Deb, K. and Jain, H. "An Evolutionary Many-Objective Optimization Algorithm Using Reference-Point-Based Non-dominated Sorting Approach, Part I: Solving Problems With Box Constraints." *IEEE Transactions on Evolutionary Computation* Vol. 18 No. 4 (2014): pp. 577–601. DOI [10.1109/TEVC.2013.2281535](https://doi.org/10.1109/TEVC.2013.2281535).
 - [24] Jain, H. and Deb, K. "An Evolutionary Many-Objective Optimization Algorithm Using Reference-Point Based Non-dominated Sorting Approach, Part II: Handling Constraints and Extending to an Adaptive Approach." *IEEE Transactions on Evolutionary Computation* Vol. 18 No. 4 (2014): pp. 602–622. DOI [10.1109/TEVC.2013.2281534](https://doi.org/10.1109/TEVC.2013.2281534).
 - [25] Blank, J. and Deb, K. "Pymoo: Multi-Objective Optimization in Python." *IEEE Access* Vol. 8 (2020): pp. 89497–89509. DOI [10.1109/ACCESS.2020.2990567](https://doi.org/10.1109/ACCESS.2020.2990567).
 - [26] Vrugt, J. A. and Robinson, B. A. "Improved Evolutionary Optimization from Genetically Adaptive Multimethod Search." *Proceedings of the National Academy of Sciences* Vol. 104 No. 3 (2007): pp. 708–711. DOI [10.1073/pnas.0610471104](https://doi.org/10.1073/pnas.0610471104).

- [27] Hadka, D. and Reed, P. "Borg: An Auto-Adaptive Many-Objective Evolutionary Computing Framework." *Evolutionary Computation* Vol. 21 No. 2 (2013): pp. 231–259. DOI [10.1162/EVCO_a_00075](https://doi.org/10.1162/EVCO_a_00075).
- [28] Das, I. and Dennis, J. "Normal-Boundary Intersection: A New Method for Generating the Pareto Surface in Nonlinear Multicriteria Optimization Problems." *SIAM Journal on Optimization* Vol. 8 No. 3 (1998): pp. 631–657. DOI [10.1137/S1052623496307510](https://doi.org/10.1137/S1052623496307510).
- [29] Hu, H., Feng, M. and Ren, T. "Effect of Taper Error on the Performance of Gas Foil Conical Bearing." *Industrial Lubrication and Tribology* Vol. 72 No. 10 (2020): pp. 1189–1197. DOI [10.1108/ILT-03-2020-0089](https://doi.org/10.1108/ILT-03-2020-0089).
- [30] Verma, S. K. and Tiwari, R. "Robust Design of Ball Bearings for an Improved Performance Using Genetic Algorithm." *International Journal for Computational Methods in Engineering Science and Mechanics* Vol. 22 No. 6 (2021): pp. 514–537. DOI [10.1080/15502287.2021.1893865](https://doi.org/10.1080/15502287.2021.1893865).
- [31] Schiffmann, J. and Favrat, D. "The Effect of Real Gas on the Properties of Herringbone Grooved Journal Bearings." *Tribology International* Vol. 43 No. 9 (2010): pp. 1602–1614. DOI [10.1016/j.triboint.2010.03.006](https://doi.org/10.1016/j.triboint.2010.03.006).
- [32] Zhang, J., Lu, L., Zheng, Z., Tong, H. and Huang, X. "Experimental Verification: a Multi-Objective Optimization Method for Inversion Technology of Hydrodynamic Journal Bearings." *Structural and Multidisciplinary Optimization* Vol. 66 No. 1 (2023): pp. 1–17. DOI [10.1007/s00158-022-03470-z](https://doi.org/10.1007/s00158-022-03470-z).

APPENDIX A. IMPELLER WHEEL CONVERSION TO CYLINDERS

A.1 Hub and blade parametrizations with piecewise functions

$$f_{\text{hub}}(z) = \begin{cases} \sqrt{r_{2h}^2 - (z - r_{2h})^2} & 0 \leq z \leq r_{2h} \\ r_4 - \sqrt{d^2 - (d^2/c^2) \cdot (z - r_{2h})^2} & r_{2h} \leq z \leq r_{2h} + c \\ r_4 & r_{2h} + c \leq z \leq r_{2h} + c + b_6 \\ r_4 - \sqrt{f^2 - (f^2/e^2) \cdot (z - L_{\text{imp}})^2} & r_{2h} + c + b_6 \leq z \leq L_{\text{imp}} \end{cases} \quad (10)$$

$$f_{\text{bld}}(z) = \begin{cases} r_4 - \sqrt{b^2 - (b^2/a^2) \cdot (z - r_{2h})^2} & r_{2h} \leq z \leq r_{2h} + c - b_4 \\ r_4 & r_{2h} + c - b_4 \leq z \leq r_{2h} + c \end{cases} \quad (11)$$

with

$$\begin{aligned} a &:= r_4/\phi - b_4 \\ b &:= r_4 - r_{2s} \\ c &:= r_4/\phi \\ d &:= r_4 - r_{2h} \\ e &:= r_4/\phi^2 - b_6 \\ f &:= r_4 - R_{\text{ROT}} \\ b_6 &:= b_6 = b_4/\phi \\ L_{\text{imp}} &:= r_{2h} + c + b_6 + e \\ \phi &:= 1.618 \end{aligned}$$

A.2 Conservation of mass and transverse moment of inertia

$$\rho_{\text{cyl},i} \cdot \pi \cdot (R_{\text{cyl},i}^2 - R_{\text{hub},i}^2) \cdot L_i = m_{\text{bld},i} \quad (12)$$

$$\frac{m_{\text{bld},i}}{12} \cdot (3 \cdot (R_{\text{cyl},i}^2 + R_{\text{hub},i}^2) + L_i^2) = I_{t,\text{bld},i} \quad (13)$$

A.3 Inertia tensor of one blade

$$\mathbf{I} = \begin{bmatrix} I_1 \cos^2 \theta + I_2 \sin^2 \theta & (I_2 - I_1) \sin \theta \cos \theta & 0 \\ (I_2 - I_1) \sin \theta \cos \theta & I_1 \sin^2 \theta + I_2 \cos^2 \theta & 0 \\ 0 & 0 & I_3 \end{bmatrix} \quad (14)$$

A.4 Transverse moment or inertia and mass of one blade

$$I_{t,i}(\theta) = I_2 \sin^2 \theta + I_1 \cos^2 \theta + m_{\text{bld},i} \left(R_{\text{hub},i} + \frac{R_{\text{bld},i}}{2} \right)^2 \cos^2 \theta \quad (15)$$

$$m_{\text{bld},i} = \rho_{\text{imp}} \cdot (e_{\text{bld}} \cdot (R_{\text{bld},i} - R_{\text{hub},i}) \cdot L_i) \quad (16)$$

A.5 Angular separation between a blade and a splitter

$$\Delta\theta = \frac{2\pi}{(N_{\text{bld}} + N_{\text{spl}})} \quad (17)$$

A.6 Transverse moment of inertia of nth blade/splitter

$$I_{t,i}(n) = I_2 \sin^2(n\Delta\theta) + I_1 \cos^2(n\Delta\theta) + m_{\text{bld},i} \left(R_{\text{hub},i} + \frac{R_{\text{bld},i}}{2} \right)^2 \cos^2(n\Delta\theta) \quad (18)$$